Computational and experimental therapeutic efficacy analysis of andrographolide phospholipid complex self-assembled nanoparticles against Neuro2a cells

Mourya, Atul; Pingle, Purva; Babu, Chanti Katta; Veerabomma, Harithasree; Sainaga Jyothi, Vaskuri G.S; Novak, Jurica; Pathak, Prateek; Grishina, Maria; Verma, Amita; Kumar, Rahul; ...

Source / Izvornik: **Biochimica et Biophysica Acta (BBA) - General Subjects, 2022, 1867**

Journal article, Accepted version
Rad u časopisu, Završna verzija rukopisa prihvaćena za objavljivanje (postprint)

https://doi.org/10.1016/j.bbagen.2022.130283

Computational and experimental analysis of self-assembled soft andrographolide phospholipid complex against Neuro2a cells

Atul Mourya[1], Purva Pingle[1], Chanti Katta Babu[1], Veerabroma Hartisree[1], Vaskuri G.S Sainaga Jyothi[1], Jurica Novak[2,3,4], Prateek Pathak[5], Maria Grishina[5], Amita Verma[6], Rahul Kumar[7], Pankaj Kumar Singh[1], Dharmendra Kumar Khatri[7], Shashi Bala Singh[7], Jitender Madan[1,*]

[1]*Department of Pharmaceutics, National Institute of Pharmaceutical Education and Research, Hyderabad, Telangana, India*
[2]*Department of Biotechnology, University of Rijeka, Rijeka, 51000, Croatia*
[3]*Center for Artificial Intelligence and Cybersecurity, University of Rijeka, Rijeka, 51000, Croatia*
[4]*Scientific and Educational Center 'Biomedical Technologies' School of Medical Biology, South Ural State University, Chelyabinsk, 454080, Russia*
[5]*Laboratory of Computational Modelling of Drugs, Higher Medical and Biological School, South Ural State University, Chelyabinsk, 454008, Russia*
[6]*Bioorganic and Medicinal Chemistry Research Laboratory, Department of Pharmaceutical Sciences, Sam Higginbottom University of Agriculture, Technology and Sciences, Prayagraj, Uttar Pradesh, India*
[7]*Department of Biological Sciences, National Institute of Pharmaceutical Education and Research, Hyderabad, Telangana, India*

Total Figures/Tables: 08

***Corresponding author**: Jitender Madan, Department of Pharmaceutics, National Institute of Pharmaceutical Education and Research, Hyderabad, Telangana, India

Email: jitenderpharmacy@gmail.com

Biochimica et Biophysica Acta (BBA) - General Subjects
Volume 1867, Issue 2, February 2023, 130283
doi: 10.1016/j.bbagen.2022.130283
web: https://www.sciencedirect.com/science/article/pii/S030441652200201X

Abstract

Background: Neuroblastoma is one of the most common malignancies in childhood, accounts for approximately 7% of all malignancies. Andrographolide (AN) inhibits cancer cells progression via multiple pathways like cell cycle arrest, mitochondrial apoptosis, NF-κβ inhibition, and antiangiogenesis mechanism. Despite multiple advantages, application of AN is very limited due to its low aqueous solubility (6.39±0.47 µg/mL), high lipophilicity (log P~2.632±0.135), and reduced stability owing to pH sensitive lactone ring.
Objectives and Results: In present investigation, a molecular complex of AN with soya-L-α-phosphatidyl choline (SPC) was synthesized as ANSPC and characterized by FT-IR and ^{1}H NMR spectroscopy. Spectral and molecular simulation techniques confirmed the intermolecular interactions between the 14-OH group of AN and the $N^+(CH_3)_3$ part of SPC. In addition, molecular dynamics (MD) simulation was used to determine the degree of interaction between various proteins such as TNF-α, caspase-3, and Bcl-2. Later, ANSPC complex was transformed in to self-assembled soft nanoparticles of size 201.8±1.48 nm with PDI of 0.092±0.004 and zeta potential of -21.7±0.85 mV. The IC50 of free AN (8.319 µg/mL) and the self-assembled soft ANSPC nanoparticles (3.406 µg/mL~1.2 µg of AN) against Neuro2a cells was estimated with significant ($P<0.05$) difference. Interestingly, the self-assembled soft ANSPC nanoparticles showed better endocytosis compared to free AN in Neuro2a cells. *In-vitro* biological assays confirmed that self-assembled soft ANSPC nanoparticles induces apoptosis in Neuro2a cells by declining the MMP (Δψm) and increasing the ROS generation.
Conclusion: Self-assembled soft ANSPC nanoparticles warrant further in-depth antitumor study in xenograft model of neuroblastoma to establish the anticancer potential.

Keywords: Andrographolide; neuroblastoma; complechixation; molecular simulation; self-assembled nanoparticles

1. Introduction

Neuroblastoma is a heterogenous sympathetic nervous system malignancy exclusively observed in early childhood [1,2]. It is one of the most common types of malignancy in childhood as neuroblastoma accounts for about 7% of all malignancies observed in children below age of 10 [3,4]. Current treatment options for patients with neuroblastoma involve application of chemotherapy such as cyclophosphamide, cisplatin, vincristine, etc. along with other approaches like surgery, neoadjuvant therapy, stem cell therapy and immunotherapy [5]. Patients with high grade neuroblastoma have a terrible prognosis with a cure rate of 20% despite advancements in radiotherapy, chemotherapy, and surgery [6]. Due in part to the detrimental effects of radiation and chemotherapy on the developing nervous system, children recuperating from neuroblastoma commonly display learning and memory problems as well as fine motor skill impairment [7]. The critical prognoses and lack of therapies consequently reduce the hope of quality life.

Among several wonder phytomolecules, andrographolide (AN), a diterpene lactone is mainly found in various parts of the plant "*Andrographis paniculata*" belonging to "*Acanthanceae*" family. Mechanistically, AN lowers NF-κB (nuclear factor kappa-light-chain-enhancer of activated B cells) activity along with reduction in expression of Bcl-2 and Bcl-xL. AN parallelly declines the phosphorylation of Akt, an essential residue for kinase activation [8, 9]. However, application of AN is very limited due to its lower water solubility (6.39 ± 0.47 μg/mL), high lipophilicity (log P~2.632 ± 0.135), and limited stability in GIT (Gastrointestinal tract) owing to pH sensitive lactone ring [9]. In addition, pharmacokinetic investigation showed oral bioavailability of 9.27 ± 1.69% with C_{max} of 0.73 ± 0.17 μM/L and T_{max} of 0.42 ± 0.14 h. The half-live ($t_{1/2}$) of AN was found to 1.86±0.21 h and 3.30±0.35 h after *i.v.* and oral administration, respectively [10]. Furthermore, quick biotransformation and efflux by P-gp (pumping glycoprotein) also lowers AN penetration and absorption [11].

Stability study conducted for powdered AN herb at room temperature suggest rapid reduction in andrographolide content (8-25%) in 3 months [12]. Besides this, presence of diterpene lactone in AN is prone to rapid transformation under higher pH and temperature conditions leading to formation of 14-deoxy-11,12-didehydroandrographolide [12,13]. Therefore, a number of attempts have been undertaken by the researchers to improve permeation and drug delivery of AN in cancer cells [14–16].

Phospholipid complex mediated nano-drug delivery technique has been widely employing to augment the permeation of phytomolecules [17–19]. Soya-L-α-phosphatidyl choline (SPC), a biocompatible component in phospholipid complex allows it to penetrate the cell membranes easily. Owing to amphiphilic nature, SPC is capable of boosting solubility of drugs, thereby improving their permeation, dissolution and oral absorption. However, conversion of unsaturated phospholipid containing formulation into dry or free flowing powder is a difficult task due to low gel to liquid crystal transition temperature (Tm) values and amorphous structure, which yield sticky powders that are challenging to deaggregate [20,21]. Due to poor dispersibility, payloads are released into aqueous fluids more slowly, which reduces the amount of therapeutic entity that is readily bio-accessible. Hence, phospholipid-drug complex does not bear desirable pharmaceutical features for its application in drug delivery.

Phospholipid-drug complex mediated soft nanoparticles have shown excellent potential as a drug delivery vehicle [22–24]. The efficient role of phospholipid nanoparticles in modifying polarity, improving the clinical utility of drugs with poor permeability and bioavailability as well as reduction in gastrointestinal toxicity is well documented [25–29].

Therefore, in present investigation, andrographolide-Soya-L-α-phosphatidyl choline (ANSPC) complex was synthesized and characterized using analytical, spectral as well as molecular docking and simulation techniques that later transformed in to self-assembled soft nanoparticles of ANSPC. The therapeutic potential of self-assembled soft ANSPC nanoparticles was examined *in-vitro* in Neuro-2a (mouse neuroblastoma) cells with well-established cell toxicity, cellular uptake and apoptosis assays.

2. Materials and methods

2.1. Chemicals and reagents

Andrographolide (IUPAC name: (3*E*,4*S*)-3-[2-[(1*R*,4*aS*,5*R*,6*R*,8*aS*)-6-hydroxy-5-(hydroxymethyl)-5,8*a*-dimethyl-2-methylidene-3,4,4*a*,6,7,8-hexahydro-1*H*-naphthalen-1-yl]ethylidene]-4-hydroxyoxolan-2-one) (95% w/w; Mw~350.455 Da) was procured from Maysar Labs, Faridabad, India. Soya-L-α-phosphatidyl choline (SPC) was purchased from TCI Chemicals (India). Dulbecco’s modified eagle medium (DMEM) and fetal bovine serum (FBS) were obtained from Gibco (Life Technologies, Thermo Scientific). MTT (3-(4,5-Dimethylthiazol-2-yl)-2,5-diphenyltetrazolium bromide), DCFDA (2’-7’-Dichlorodihydrofluorescein diacetate), JC-1 (5,5,6,6’-Tetrachloro-1,1’,3,3’-tetraethylbenzimidazoylcarbocyanine iodide) were obtained from Sigma-Aldrich (St. Louis, MO, USA). Other solvents and reagents were of higher analytical grades and purchased from authorized local distributors.

2.2. Synthesis and spectral characterization of andrographolide-Soya-L-α-phosphatidyl choline complex

The ANSPC complex was synthesized by solvent evaporation method [30]. In brief, calculated quantity of AN (0.0175 g or 1 mM) and SPC (0.0322 g or 1 mM) was weighed and poured in 50 mL of ethyl alcohol (100%) contained in a round bottom flask. The mixture was continuously stirred for 3 h at 60˚C. The resulting solution was subjected to rotary evaporator for ethanol removal, and the dried residue was collected and stored in a suitable air tight container for spectral analysis. The FT-IR spectrum of AN, SPC, physical mixture and ANSPC complex was recorded using Spectrum Two spectrophotometer (Perkin Elmer, USA). To minimize the level of noise in spectra, background scanning was performed prior to spectra recording. All the spectra were measured from 400-4000cm^{-1} with resolution of 4 cm^{-1}. In addition, ^{1}H NMR spectroscopy of AN, SPC, physical mixture and ANSPC complex was carried out using Bruker DPX-500 MHz (Bruker, Argentina). To record the spectrum, 5 mg/ml solution of AN, physical mixture and ANSPC was made in deuterated DMSO (DMSO-d6) whereas SPC was dissolved in $CDCl_3$. All the measurements were conducted using tetramethyl silane (TMS) as internal standard while maintaining the temperature at 295.2 K.

2.3. Computational characterization of andrographolide-Soya-L-α-phosphatidyl choline complex

2.3.1. Construction of andrographolide and soya-L-α-phosphatidyl choline molecules

The initial 3D geometry of the SPC molecule was extracted from the crystal structure of human phosphatidylcholine transfer protein (PDB ID: 1LN1). The atomic coordinates of the AN molecule were downloaded from the PubChem database (PubChem CID 5318517) [31]. Both molecules were optimized using the B3LYP/6-311+g (d,p) level of theory [32]. On the other hand, for AN molecule, default convergence criterion was used due to flexibility and high number of single rotatable bonds. In case of SPC, looser criteria were used in geometry optimization process. For minimum energy structures, the atomic charges were calculated following CHELPG (Charges from Electrostatic Potentials using a Grid based method) fitting protocol to reproduce the molecular electrostatic potential [33]. The optimized geometries and atomic charges of AN and SPC were used in the procedure for generating force field parameters. The parametrization was performed using the *Antechamber* module of Amber molecular dynamics package and general Amber force field (GAFF) [34–36].

2.3.2. Generation of the structure of the andrographolide-Soya-L-α-phosphatidyl choline complex

Gaussian-accelerated molecular dynamics (GaMD) was applied to sample the binding modes between AN and SPC in the non-covalent complex, ANSPC. The minimum energy structures of the AN and SPC were placed with random orientations and the distance between the centroids of these two molecules was 20.4 Å. The non-covalent complex was solvated in a truncated octahedral box with TIP3P (transferable intermolecular potential 3P) water molecules spanning a 10 Å thick buffer [37]. In total, 3306 water molecules were added. As a first step, 2000 minimization cycles (1500 steepest descent + 500 conjugate gradient) were performed for minimizing only water molecules, followed by 2000 minimization cycles (1500 steepest descent + 500 conjugate gradient) of the whole box. The system was heated from 0 K to 310 K and equilibrated for 5 ns in the NPT ensemble (p=1 bat, T=310 K). 2 ns conventional molecular dynamics simulation was performed to collect maximum, minimum, average and standard deviation of the potential energies, parameters needed to run GaMD. After 50 ns GaMD equilibration, 1.9 microsecond GaMD production simulation of ANSPC complex was performed. In total 190,000 frames were generated.

2.3.3. Molecular docking

The 3D structures of the tumor necrosis factor alpha (TNF-α, PDB ID: 2AZ5), the caspase-3 (PDB ID: 3EDQ) and B-cell lymphoma 2 (Bcl-2, PDB ID: 6UVE) proteins were obtained from RCSB protein database [38]. Prior to docking, water and all other small molecules were removed. For TNF-α and caspase-3, chains A and B were retained, while for Bcl-2 only, chain C was retained. Missing residues were modelled using Šali and Bundell’s Modeller accessed through the UCSF Chimera 1.14. [39,40].To prepare targets and ligand (ANSPC complex) for molecular docking, all non-polar hydrogen atoms were merged, Gasteiger charges were added using AutoDock Tools (ADT) and the structures were saved in pdbqt format. Molecular docking simulations were performed in AutoDock Vina [41]. The center of the grid boxes was set at the CB atom type of Tyr119 of TNF-α (-3.4, -0.8, -5.0 Å), SG atom type of Cys163 of Bcl-2 (-5.9, 0.8, -10.4 Å) and O atom type of Gly138 of caspase-3 (8.6, 7.3, -4.4 Å). The size of the box was 40×40×40 $Å^3$, while number of modes and exhaustiveness were both set to 100.

2.3.4. Molecular dynamics simulations

Two sets of molecular dynamics (MD) simulations were performed; the first set for free, unbound protein (denoted with prefix, APO-) and the second set for the proteins with ANSPC complex bound to it (denoted with ANSPC). Initial structures of APO-proteins were downloaded from the RCSB protein database. Water and small molecules were deleted, while missing residues for selected chains were modelled using Modeller, as described in previous section. After careful analysis of docking results and visual inspection, the ANSPC complex with the best docking score for each of three targets was selected. They served as initial structures for subsequent ANSPC complex-protein MD simulations. The titrations states and the protonation of the proteins side chain residues were performed using PDB2PQR web-server [42]. The proteins were treated using the AMBER ff14SB force field, and ANSPC complex using GAFF [43]. All systems were solvated in a truncated octahedral box of TIP3P water molecules in a way that the distance between the outermost ANSPC-enzyme atoms and the box wall was 12 Å. The systems were neutralized by adding Na^+ or Cl^- ions at 0.15 M concentration [44]. The minimization-equilibration-production protocol was same for all the simulations. First, the system was minimized in 10,000 cycles (4000 steepest descent + 6000 conjugate gradient) and both the protein and ligand was restrained ($k = 10.0$ kcal mol^{-1} $Å^{-2}$). Then, the whole system was gradually heated form 0 K to 310 K in 500 ps without any restrains. After heating process, the system was equilibrated under NPT ensemble for 500 ps. Finally, the production run was simulated for 200 ns. A Langevine thermostat with collision frequency of 1 ps^{-1} was used to control the temperature. The pressure was set to 1 bar, time step to 2 fs, and in all simulations hydrogen atoms were constrained using the SHAKE algorithm [45]. The cut-off distance for non-bonded interaction was 11 Å, while particle mesh Ewald method was used to treat long-range electrostatic interactions [46]. Periodic boundary conditions were employed. All MD simulations were performed using Amber molecular dynamics package [35].

2.3.5. Calculation of binding free energies

The binding free energies between ANSPC complex and proteins were calculated by well-established scheme, known as molecular mechanics/generalized Born surface area (MM/GBSA) method. The binding free energy (ΔG_{bind}) formula in MM/GBSA formalism and with the single-trajectory protocol is implemented in Amber package and equals

$$\Delta G_{bind} = G_{complex} - (G_{receptor} + G_{ligand}) \quad (1)$$

Where, $G_{complex}$, $G_{receptor}$, and G_{ligand} are averaged over snapshots extracted from the production MD trajectory. The MMPSBA.py script was used to estimate binding free energies of the ligand-protein complexes. For all protein-ligand complexes, the production phase trajectory was divided into 4 parts of 50 ns length. Final ΔG_{bind} was calculated for all 4 parts of the simulations as average value over 100 snapshots extracted from 50 ns part. The final ΔG_{bind} was reported as mean ± standard deviation (SD) of all 4 parts. The calculated MM/GBSA binding free energies were decomposed into specific residue contribution on a per-residue basis. In this way, the contributions to ΔG_{bind} arising from each amino acid side chains were obtained and the nature of the energy change in terms of interaction and solvation energies, or entropic contributions were identified. Entropy term was estimated based on 50 snapshots per 50 ns set, and reported value is an average over 4 sets.

2.4. Preparation and characterization of self-assembled soft nanoparticles of andrographolide-Soya-L-α-phosphatidyl choline complex

2.4.1. Preparation of self-assembled soft nanoparticles

The self-assembled soft nanoparticles of ANSPC complex were formulated using nanoprecipitation method [22]. Briefly, a clear solution containing ANSPC was produced by properly weighing 10 mg of the ANSPC complex and mixing it with 10 mL of dichloromethane by employing magnetic stirrer. The organic phase containing ANSPC complex was added dropwise (0.5 mL/min) into distilled water (40 mL) maintained at continuous stirring (1000 rpm) followed by controlled evaporation of organic phase to obtain suspension of self-assembled soft ANSPC nanoparticles. The resultant suspension was subjected to freeze-drying under the conditions of controlled condenser temperature of -50°C and vacuum of 10 Pa. Finally, the lyophilized suspension of self-assembled soft ANSPC nanoparticles was stored at 4°C until further use.

2.4.2. Drug content evaluation

To determine the AN content in self-assembled ANSPC nanoparticles, assay was performed using previously developed HPLC method [10]. In brief, approximately 25 mg of lyophilized self-assembled nanoparticles was dissolved in 5 mL of ethanol. The obtained suspension was subjected to centrifugation at 10,000 rpm for 15 min at room temperature. The resultant supernatant was collected, filtered through 0.22-µm syringe filter and after appropriate dilution, 10 µL was injected into HPLC for quantification of AN.

Drug content = Amount of AN recovered/ Amount of Nanoparticles (2)

2.4.3. Particle size, zeta potential and shape analysis

The mean particle size and surface charge of self-assembled soft ANSPC nanoparticles was measured by the dynamic light scattering (DLS) using Nano Zeta Sizer (Nano ZS, Malvern instrument Corporation, UK). The samples were suitably diluted with deionized water to maintain the count rate in the range of 250-400 kcps. The analysis was performed at backscattered light detector angle of 173˚ while maintaining the temperature at 25˚C. On the other hand, surface topography of self-assembled soft ANSPC nanoparticles was analyzed by transmission electron microscopy (Jeol, 120 KV) equipped with bottom mounted 11 MP digital CCD camera (EMSIS, Quemesa). The sample was placed on copper grid and stained with 2% aqueous uranyl solution. Excess stain was removed with filter paper and sample was dried at room temperature and observed under TEM.

2.5. Therapeutic efficacy evaluation of self-assembled soft nanoparticles of andrographolide-Soya-L-α-phosphatidyl choline complex: In-vitro analysis

2.5.1. Cell viability assay

Neuro2a cells were seeded in a 96-wells plate with a cell density of $5x10^3$ cells/well, incubated for 24 h at 37°C. Next day, a complete medium containing 10% FBS was replaced with incomplete medium (without FBS) and further incubated for 24 h in CO_2 incubator. Later, Neuro2a cells were treated with AN (1.25 µg/mL to 80 µg/mL in DMSO) as well as self-assembled soft ANSPC nanoparticles (1.25 µg/mL to 40 µg/mL in DMSO). The cells were incubated for 48 h followed by addition of 100 µL MTT (5 mg/mL) and further incubated for 4 h. After incubation, supernatant was discarded and formazan crystals were dissolved in 150 µL of DMSO. The absorbance of each well was determined at 590 nm using EnVision multimode plate reader (Perkin Elmer, Massachusetts, USA).

2.5.2. Analysis of cellular reactive oxygen species level

The production of cellular reactive oxygen species (ROS) was estimated in Neuro2a cells according to protocol of *Park et al.,* with some modification [47]. Briefly, cells were seeded in a 6-wells plate at a density of $5x10^6$ cells/well. After 24 h, cells were pre-incubated in FBS free medium for 12 h followed by treatment with AN (10 µg/mL in DMSO) and self-assembled soft nanoparticles of ANSPC (2.5 µg/ML and 5 µg/ML) and subjected to incubation for 24 h. The production of ROS was measured by incubating cells with DCFDA (10 µg/ml) for 30 min. Later, cells were washed three times with cold PBS (pH~7.4) and the images were captured using Nikon inverted fluorescence microscope (Nikon, Japan).

2.5.3. Measurement of mitochondrial membrane potential

This assay was performed according to already reported method by *Tang et al.*, with slight modifications [48]. Briefly, 5x10^6 Neuro2a cells per well in a 6-wells plate were treated with AN (10 µg/mL in DMSO) and self-assembled soft nanoparticles of ANSPC (2.5 µg/mL and 5 µg/mL in DMSO) and incubated in a CO_2 incubator for 24 h. After incubation, medium was removed and cells were washed with cold PBS (0.1 M, pH~7.4) followed by incubation with JC-1 dye (10 µM/mL) (cationic carbocyanine dye) for 30 min. Later images were captured with an inverted fluorescence microscope (Nikon, Japan).

2.5.4. Cell uptake assay

Neuro2a cells were seeded on poly-L-lysine coated coverslips in a 6 wells cell culture plate at the density of 5x10^6 cells/well. After reaching 70% confluency, the complete medium was replaced with FBS-free DMEM medium and incubated for 24 h. This was followed by treatment with AN (10 µg/mL in DMSO) and self-assembled soft nanoparticles of ANSPC (2.5 µg/mL and 5 µg/mL in DMSO) and again incubated for 24 h. Later cells were washed with cold PBS (0.1 M, pH~7.4) and fixed in 4% paraformaldehyde for 20 min. The cover slip was fixed with glycerin and cell images were captured with an inverted Nikon fluorescence microscope (Nikon, Japan). Excitation and emission filters 494 nm and 518 nm were used for FITC (Fluorescein isothiocyanate) and the images were captured using NS Elements Software [49].

2.5.5. Quantification of cell death by apoptosis assay

This assay was performed as previously described by *Sriwastva et al.*, with little modifications [50]. Briefly, Neuro2a cells were seeded in a 6 wells plate (5x10^6 cells/well) and incubated at 37˚C followed by treatment with AN (10 µg/mL in DMSO) and self-assembled soft nanoparticles of ANSPC (2.5 µg/mL and 5 µg/mL in DMSO). After 24 h of incubation, medium was removed and cells were washed with cold PBS (pH~7.4) and then fixed in 4% paraformaldehyde for 10 min. Cells were stained with dual fluorescent staining solution (10-µL) which is the mixture of 100 µg/mL AO (Acridine orange) and 100 µg/mL EtBr (Ethidium bromide) added to each well and incubated for 5 min at room temperature. The filter with excitation and emission at 494 nm and 518 nm for AO and EtBr were used, respectively. The morphology alteration of the apoptotic cells was quantified and 500 cells were counted within 20 min using an inverted fluorescent microscope (Nikon, Japan).

2.6. Statistical analysis

Statistical significance was analyzed with one-way analysis of variance and student t test with $p<0.05$ as a significant level of difference. The results are presented as the mean ± square root of variance for $n=3$.

3. Results and Discussion

3.1. Synthesis and spectral characterization of ANSPC complex

Studies suggest that drug-phospholipid complex may considerably enhance the solubility, gastrointestinal stability, permeability as well as therapeutic efficacy of drugs [51,52]. In present study, we have synthesized ANSPC complex using solvent evaporation method [30]. The dried yellow coloured sticky mass of ANSPC complex was stored at room temperature in a tightly closed container. To corroborate the interaction between AN and SPC, spectral techniques like FT-IR and ^{1}H NMR spectroscopy were employed. FT-IR spectrum of AN exhibits characteristic peaks at 3392 cm^{-1} (-OH group), 2915 cm^{-1} (-CH_2/CH_3 groups), 1722 cm^{-1} (-C=O, lactone ring) and 1455 cm^{-1} (-C=C) (**Suppl. Figure 1**) whereas SPC demonstrated peaks at 1737 cm^{-1} (-C=O), 1052 cm^{-1} (P-O-C) and 973 cm^{-1} ($N^+(CH_3)_3$) [53]. All the major characteristic peaks for AN and SPC were retained in physical mixture. However, ANSPC spectrum displayed broadening of -OH peak (3392 cm^{-1}) indicating weak intermolecular interaction between AN and SPC (**Suppl. Figure 1**)[54].

Apart from this, vibrational spectrum for ANSPC complex obtained by GaMD simulation was calculated. The wavenumbers of the vibrational modes together with associated intensities were derived in the harmonic approximation on the B3LYP/6-311+g (d,p) level of theory. In general, good agreement between predicted and experimental IR spectrum was obtained (**Figure 1**). Predicted spectrum was slightly shifted to higher wavenumbers. The shift was most pronounced for O-H and C=O stretching vibrations, that have been up-shifted by almost 350 cm^{-1} and 90 cm^{-1}, respectively. Besides a harmonic effect that has neglected, intramolecular bonding (like hydrogen bond), coupling between normal modes and existence of several conformer could explain observed discrepancies [55].

In addition, ^1H NMR spectrum of AN, SPC, physical mixture and ANSPC complex is represented in **Figure 2**. ^1H NMR spectrum of AN depicts characteristic peaks for $-C=CH_2$ (δ=6.62 ppm), 14-OH (δ=5.72 ppm), 19-OH (δ=4.81 ppm) and 3-OH (δ=4.62 ppm) (**Figure 2 and Suppl. Figure 2**). Besides this, in SPC spectrum, characteristic peaks were observed for saturated aliphatic chain i.e., $-CH_2$ and $-CH_3$ (δ=1.00-1.80 ppm), $N^+(CH_3)_3$ (δ=3.32 ppm) and unsaturated aliphatic chain (δ=5.36 ppm). The physical mixture shows presence of all the characteristic peaks for AN and SPC, whereas ANSPC spectrum indicates disappearance of 14-OH (δ=5.72 ppm) of AN and shifting in $N^+(CH_3)_3$ (δ=3.32 ppm to 3.24 ppm) peak belonging to SPC, consistent to the previous report [54]. On the other hand, peaks for 3-OH and 19-OH of AN and aliphatic chain of SPC were appeared prominent and suggested the intermolecular interaction between AN and SPC as predicted from molecular modelling.

3.2. Computational characterization of ANSPC complex: Structural and therapeutic efficacy interpretation

3.2.1. Prediction of molecular structure of ANSPC complex

The structure of ANSPC complex is unknown. Recently, it was published that phospholipid and gallic acid are combined by non-covalent interactions [56]. To obtain 3D structure of

ANSPC complex, GaMD was performed. GaMD is a robust computational method for unconstrained enhanced sampling of biomolecules [57]. It enables acceleration of biomolecular simulations by orders of magnitude by adding a harmonic boost potential and reducing energy barriers. From 1.9 µs GaMD simulation of ANSPC complex, 190,000 structures of the complex were collected. Following recommendations of Wu *et al.*, we monitored the centroid distance between AN and SPC (**Figure 3A**), to select the most appropriate geometry [58].Only 1333 structures (0.7%) had the centroid distance below 3.0 Å. The frame with the lowest centroid distance was selected as the most appropriate geometry of the ANSPC complex (**Figure 3 B**), and the distance between the centroids was 0.76 Å. For xyz coordinates of the selected ANSPC complex, see **Suppl. Table 1**. The hydrophobic part of the AN molecule was partially surrounded by the non-polar part of the SPC molecule, i.e., the fatty chains. Nevertheless, there was one hydrogen bond of 2.28 Å long between hydroxyl group from five-membered ring of AN and oxygen atom from phosphate group of SPC molecule (**Figure 3B**), consistent to the ^{1}H NMR spectroscopy data (**Figure 2**).

We were interested whether the before-mentioned hydrogen bond, together with hydrophobic interactions between AN and SPC molecules, were strong enough in the non-covalent ANSPC complex to exist as one entity when the ANSPC complex was bound to the protein. The second question we want to address was how the ANSPC complex bound to the protein changes its stability. To answer these questions, molecular docking and MD simulations were performed. The first set of MD simulations included three proteins, namely tumor TNF-α, the caspase-3 and Bcl-2, in their apo-form, i.e., in the free, unbound form (denoted with prefix APO-). In the second set, ANSPC complex was bound to the protein. Initial structures for ANSPC-TNF-α (**Suppl. Figure 3**), supported information for ANSPC-caspase-3 (**Suppl.**

Figure 4) and ANSPC-Bcl-2 (**Figure 4**) were obtained by docking of the ANSPC complex using GaMD simulation to the Apo-form of selected proteins.

3.2.2. Binding of ANSPC complex to TNF-α

In **Suppl. Figure 3C,** changes in RMSD (Root-mean-square deviation) of the atoms forming protein backbone compared to the first frame are displayed, both for Apo-TNF-α and ANSPC-TNF-α. It was appeared that the changes in RMSD values are relatively small, ruling out significant changes in the geometry. In the second half of the trajectory, the RMSD of Apo-TNF-α is constantly higher compared to the RMSD of ANSPC-TNF-α. Additional proof for the stability of both systems are minimal changes in the radius of gyration (**Suppl. Figure 3D**). The analysis of the RMSF (Root-mean-square fluctuations) (**Suppl. Figure 3E**) provided some insight about involvement of specific amino acids in stability of the complex along the MD trajectory. The residues between Gln102 and Trp114 in both chains show the highest flexibility. These amino acids are part of an unstructured loop connecting two β-sheets. Two more unstructured loops deserve special attention; Arg32-Leu37 and Tyr141-Gln149 regions. These regions are becoming less flexible upon binding of the ANSPC complex to the TNF-α. Average RMSF values for apo-TNF-α and ANSPC-TNF-α corroborate lower flexibility after binding the ANSPC complex. **Suppl. Figure 3F** shows structures of TNF-α from the crystal structure (**red**), and the final structures from 200 ns MD simulations of Apo- (**sea green**) and ANSPC-TNF-α (**blue**). On the scale of the entire protein, the secondary structure was conserved upon ANSPC complex binding, with the largest changes occurring in the regions of unstructured loops. The ANSPC complex itself underwent the greatest changes within simulated time of 200 ns it dissociates (**Suppl. Figure 3 B**). SPC remained bound in the hydrophobic cleft on the contact surface between two protomers, while AN is no longer encircled by fatty acids. Now is bound to the surface of protein mainly by hydrophobic interactions and a hydrogen bond, with the hydroxyl group of

Tyr151, serving as a proton acceptor. The binding energy within MM/GBSA formalism is -66.4 ± 3.6 kJ mol^{-1}, without entropy contribution. TΔS term equals -32.7 ± 1.5 kJ mol^{-1} kJ mol^{-1} for T = 310 K. MM/GBSA binding free energies decomposition into specific residue contribution on a per-residue basis identified residues Tyr59 and Tyr119 as the most contribution to the total free binding energy, with average contribution below -3 kcal mol^{-1}.

3.2.3. Binding of ANSPC complex to Caspase-3

The analysis of RMSD and radius of gyration of caspase-3 in the Apo- and complexed forms (**Suppl. Figure 4 C and D**) confirmed stability of the protein and minimal geometrical changes during 200 ns dynamics. Overlapped crystal structure and structures from MD simulations support those findings. Secondary structure is well conserved again with the biggest difference in the regions of unstructured loops (**Suppl. Figure 4 F**). Binding of ligand has minor influence on the flexibility of the residues (**Suppl. Figure 4 E**). Nevertheless, the region around α-helix (Phe27-Met33) becomes less flexible upon ligand binding, because, as our simulations revealed, is in direct interaction with the fatty acid part of the ANSPC complex. Independent to the presence of the ligand, *C*-terminus of A chain and *N*-terminus of B chain possess highest level of flexibility. The geometry of the ANSPC complex itself underwent through significant changes throughout the trajectory (**Suppl. Figure 4A and 4B**). AN is no longer enclosed by fatty acid. Hydrogen bond with phosphate group is broken, but new hydrogen bond with one carbonyl oxygen atom is formed. 5-membered ring is oriented towards hydrophilic part of the protein. Fatty acid part of SPC has ‘unwind’ and interacts with hydrophobic part of the protein (**Suppl. Figure 4 B**). The binding energy calculated by equation, as specified, is -34.5 ± 3.4 kJ mol^{-1}, but if entropic contribution is included, then the binding energy is only -1.7 kJ mol^{-1}. Caspase-3 residues Tyr165 and Phe217 contribute most to the binding energy. Both residues have Van der Waals contacts with one or both fatty chains of SPC, while Phe217 has additional hydrophobic interactions with AN molecule.

3.2.4. Binding of ANSPC complex to Bcl-2

Compared to TNF-α and caspase-3, ANSPC complex binding to Bcl-2 has the greatest effect on dynamics of the protein (**Figure 4 A-F**). It was appeared that RMSD values for the Apo form are higher as compared to ANSPC-Bcl-2. On the other hand, radius of gyration is approximately 2Å lower for Apo-Bcl-2. From visualization and the overlay of the crystal structure and the end-point structures from MD simulations, it is easy to find structural foundations for trends observed in RMSD and radius of gyration. Only three central α-helixes remained in their conformations, due to attractive interactions between them and short β turns connecting them. First α-helix from the *N*-terminus side of the Apo-Bcl-2, the one that is approximately perpendicular to before-mentioned helices and interacts with other protomer in the crystal structure, during 200 ns simulations reorients and moves closer to Ser112. However, in case of ANSPC complex binding to Bcl-2, differences compared to the crystal structure are minor, and include dominantly changes in the *C*-terminus of the protein. Enormous difference between the crystal structure and the structure from the simulation of Apo-Bcl-2 lays in the fact that crystal structure has a potent benzoylurea inhibitor bound to it [59]. Average RMSF for Apo-Bcl-2 is for 0.28 Å higher than average RMSF for ANSPC-Bcl-2. Both values are for minimum 0.4 Å higher than corresponding values for TNF-α and caspase-3 proteins. Fatty acid part of the SPC is stretched when compared to initial (docked) structure, stretching throughout the hydrophobic region of the protein. This conformational change allowed AN to break free from phosphate group. Although the ANSPC complex dissociated after binding, both AN and SPC molecules stayed bound at the surface of the protein. The binding energy was estimated to be -66.4 ± 3.6 kJ mol^{-1}. TΔS term equals -44.6 ± 10.3 kJ mol^{-1}, making total binding energy -21.8 kJ mol^{-1}. For the first 100 ns of simulation, hydrophobic Leu55 and Leu77 residues have dominant role in ANSPC complex binding to the Bcl-2 protein, mainly by interaction with hydrophobic fatty acid chain. In addition to the

Leu77, due to conformational change in SPC during dynamics, Arg86 and Phe93 gained the importance in binding of SPC molecule during the last 100 ns part of the trajectory.

3.3. Self-assembled soft nanoparticles of ANSPC complex potently induced apoptosis in Neuro2a cells

Post characterization of ANSPC complex using spectral and MD simulation techniques, it was essential to showcase its potential in inhibiting the *Neuro2a cells* under a set of stringent biological assays. Hence, ANSPC complex was further transformed in to self-assembled soft nanoparticles using nanoprecipitation method [22]. Initially, the drug content in self-assembled soft nanoparticles of ANSPC complex was estimated. A representative chromatogram of AN displaying AN peak at 6.4 min is presented in **Suppl. Figure 5**. Assay of self-assembled soft ANSPC nanoparticles indicates presence of 8.922±0.48 mg of AN in 25 mg of nanoparticles in addition to stability of AN in tailored nanoparticles. DLS measurement of self-assembled soft ANSPC nanoparticles depicts average particle size of 201.8±1.48 nm with PDI of 0.092±0.004 and zeta potential of -21.7±0.85 mV (**Figure 5 A-C**). The photomicrograph of self-assembled soft ANSPC nanoparticles under TEM exhibited particle size of approximately >250 nm with perfect spheres. Nanoparticles found in the size range of 250 nm have demonstrated optimal phagocytosis as compared to 120 to 150 nm size range nanoparticles that exhibited uptake via clathrin or caveolin-mediated endocytosis. The maximum size of nanoparticles followed this pathway of uptake, reported to be of 200 nm [60,61]. Hence, a particular type of nanoparticles may choose and utilize multiple endocytic pathways in cancer cells depending on its size. The zeta-potential of ≥±25 mV is mostly expected as appropriate for stabilizing the nanoparticles [62]. The surface charge urbanized on the exterior results in nanoparticle repulsion, which further precludes the aggregation process [63]. Hence, surface charge of self-assembled soft ANSPC nanoparticles was appropriate to impart the stability to nanoparticles dispersion.

The therapeutic efficacy of self-assembled soft ANSPC nanoparticles was analyzed *in-vitro* using Neuro2a cells. The standard cell proliferation assay in Neuro2a cells indicated the IC_{50} of AN solution equivalent to 8.319 µg/mL significantly (Unpaired t test, $P<0.05$) higher than 3.406 µg/mL (~1.2 µg of AN) of self-assembled ANSPC nanoparticles (**Suppl. Figure 6**). Therefore, self-assembled soft ANSPC nanoparticles had better activity against the growth of Neuro2a cells in contrast to pure AN.

Next, the effect of free AN and self-assembled soft ANSPC nanoparticles treatment on ROS production was quantified using the DCFDA dye in Neuro2a cells. The green fluorescence intensity indicates the production of ROS and fluorescence intensity is directly proportional to the ROS production. The result of the study represented in **Figure 6 A-B**, revealed significant increases in green fluorescence intensity after treatment with self-assembled soft ANSPC nanoparticles as compared to free AN (~10 µg/mL) at both 2.5 µg/mL and 5 µg/mL concentrations. The green fluorescence intensity was remarkably increased post high dose treated Neuro2a cells as compared to the low dose of self-assembled soft ANSPC nanoparticles treated cells. This increase in the production of ROS further causes detrimental effects on mitochondria and leads to cell death [64]. Similarly, the effect of free AN and self-assembled soft ANSPC nanoparticles treatment on MMP ($\Delta\psi m$) was quantified using JC-1 dye **(Figure 6B)**. Under the microscope, depolarization in cells was observed as a red fluorescence. The results indicated a significant reduction in fluorescence intensity post AN and self-assembled soft ANSPC nanoparticles (low and high dose) treatment as compared to the control experimental cells (**Figure 6B**). The results of both experiments demonstrated that self-assembled soft ANSPC nanoparticles had a potent impression on ROS and MMP ($\Delta\psi m$) as compared to free AN.

Nanomedicines owing to sub-micron size exhibit the influential therapeutic potential post endocytosis into cancer cells in comparison to pure chemotherapeutic agents. Hence, the cellular uptake assay of AN and self-assembled soft ANSPC nanoparticles was carried out in Neuro2a cells. A robust and remarkable (One-way ANOVA test, $P<0.05$) increase in fluorescence intensity after treatment with low (2.5-µg/mL) and high (5-µg/mL) concentration of self-assembled soft ANSPC nanoparticles treated cells was noticed as compared to free AN (10-µg/mL) (**Figure 7 A-B**). The data indicated that Neuro2a cells treated with self-assembled soft ANSPC nanoparticles demonstrated greater accumulation as compared to free AN.

Parallelly, the Neuro2a cells were incubated with free AN and self-assembled soft ANSPC nanoparticles, fluorescently labelled with hydrophobic dyes, such as AO/EtBr. The nucleus was stained green by AO and red with EtBr. The visual fluorescence microscopy images were captured to study the cellular uptake by Neuro2a cells. EtBr was selectively taken up by non-viable cells and emited red fluorescence while AO was taken up by both viable and non-viable cells and emitted green fluorescence. Results presented in **Figure 8**, suggested the presence of healthy Neuro2a cells in control group whereas signs of nuclear constriction and early apoptosis character was noticed in AN and self-assembled soft ANSPC nanoparticles treated cells. However, level of apoptosis in self-assembled soft ANSPC nanoparticles treated cells was more prominent than free AN treated Neuro2a cells. Hence, analysis of extent of toxicity, apoptosis, MMP ($\Delta\psi m$) and cellular uptake indicated the delivery of a therapeutic concentration of self-assembled ANSPC nanoparticles in the cytoplasm of Neuro2a cells that consequently triggered a higher degree of apoptosis as compared to free AN solution.

The bulk of phospholipids in cell membrane is mainly comprises of phosphatidylcholine and phosphatidylethanolamine. Altered phospholipid membrane content, phospholipid metabolite levels, and fatty acid profiles have been implicated as markers of cancer development and progression [65]. In both healthy and malignant cells, type IV P-type ATPases work to establish plasma membrane asymmetry by transporting certain phospholipid substrates rather than cations [66]. Hence, we suppose that Type IV P-type ATPase in Neuro2a cells might have augmented the uptake of self-assembled soft ANSPC nanoparticles due to presence of phospholipid. Upon reaching to the cytoplasm in a considerably high concentration as compared to free AN, ANSPC nanoparticles subsequently triggered the apoptosis mechanism at a very low concentration. In general, moderate amount of ROS activates the mitogen-activated protein kinase/extracellular signal-regulated protein kinase 1/2 (MAPK/ERK1/2), p38, c-Jun N-terminal kinase (JNK), and phosphoinositide-3-kinase/protein kinase B (PI3K/Akt), which in turn activates the NF-κB, matrix metalloproteinases (MMPs), and vascular endothelial growth factor (VEGF) [67]. However, at high concentration, ROS causes apoptosis in cancer cells owing to DNA damage, lipid peroxidation, and protein oxidation [68]. Moreover, decrease in MMP ($\Delta\psi_m$) level also augments ROS level in cancer cells. Depolarization below a certain MMP ($\Delta\psi_m$) level may indicate impaired mitochondrial function and is a prerequisite for mitophagy and ROS generation [67]. Moreover, ANSPC in self-assembled soft nanoparticles was also predicted to bind to TNF-α (**Suppl. Figure 3**) which ultimately elevates its level to stimulate lymphocytes against Neuro2a cells. In addition, ANSPC was also predicted to bind to caspase-3 and Bcl-2 (**Suppl. Figure 4 and Figure 4**), which are important markers of apoptosis. Therefore, evidences demonstrated that self-assembled ANSPC nanoparticles owing to high uptake via type IV ATPase in addition to multiple uptake mechanism due to sub-micron size (201.8±1.48 nm) in Neuro2a cells delivered a therapeutic concentration in cytoplasm that ultimately triggered mitochondrial, death receptor, and ER (Endoplasmic reticulum) pathways of apoptosis.

4. Conclusion

In summary, computational as well as spectroscopic analysis suggest intermolecular interaction between hydrophilic head of phospholipid and hydroxy group on lactone ring leads to formation of ANSPC complex. In addition, molecular docking and MD simulation of the ANSPC complex bound to the Bcl-2, caspase-3 and TNF-α receptors allowed to estimate the stability of the ligand-protein complex and free energy of binding as well as to gain insight into the interaction network. The results from *in-vitro* and *in-silico* evaluation indicated a loss of MMP (Δψm) with concomitant increase in ROS generation as major factor leading to cell apoptosis in self-assembled soft ANSPC nanoparticles treated Neuro2a cells. Therefore, the present study of self-assembled soft ANSPC nanoparticles warrants further in-depth antitumor study in xenograft model of neuroblastoma to establish its anticancer potential.

Declaration of Competing Interest

The authors declare that they have no known competing financial interests

Acknowledgements

Authors from National Institute of Pharmaceutical Education and Research-Hyderabad, Telangana, India are highly thankful to Department of Pharmaceuticals, Ministry of Chemicals and Fertilizers, Government of India, New Delhi for providing financial assistance to carry out this work. The part of the work of Dr. Maria Grishina and Dr. Prateek Pathak is supported by the Ministry of Science and Higher Education of Russia (Grant FENU-2020-0019). Dr. Jurica Novak thanks the University of Zagreb University Computing Center (SRCE), for granting access to the Isabella computer cluster.

References

[1] Whittle SB, Smith V, Doherty E, Zhao S, McCarty S, Zage PE. Overview and recent advances in the treatment of neuroblastoma. Expert Rev Anticancer Ther. 17 (4), 2017; 369–386. https://doi.org/10.1080/14737140.2017.1285230.

[2] Smith V, Foster J. High-Risk Neuroblastoma Treatment Review. Children (basel). 5 (9), 2018; 114.https://doi.org/10.3390/CHILDREN5090114.

[3] Starchenko II, Dyachenko LV., Prylutskyi OK, Vynnyk NI, Filenko BM. The observation of congenital retroperitoneal large size neuroblastoma. Exp Oncol. 41 (2), 2019; 179-181. https://doi.org/10.32471/exp-oncology.2312-8852.vol-41-no-2.13321.

[4] Forouzani-Moghaddam MJ, Nabian P, Gholami A, Dehghanbaghi N, Azizipanah M, Jokar K, Eslami M, Zahra K, Tamehri B, Zare N, Heydari SS, Marzieh Esmaelli KN, Boyerhasani M,

Zare ZH. A review of neuroblastoma: prevalence, diagnosis, related genetic factors, and treatment. Iran J Ped Hematol Oncol. 8(4), 2018; 237–46.

[5] Swift CC, Eklund MJ, Kraveka JM, Alazraki AL. Updates in diagnosis, management, and treatment of neuroblastoma. Radiographics. 38 (2), 2018; 566-580. https://doi.org/10.1148/rg.2018170132.

[6] Schmidt ML, Lukens JN, Seeger RC, Brodeur GM, Shimada H, Gerbing RB, Stram DO, Perez C, Haase GM, Matthay KK. Biologic factors determine prognosis in infants with stage IV neuroblastoma: A prospective Children's Cancer Group study. J Clin Oncol. 18(6), 2000; 1260-1268. https://doi.org/10.1200/JCO.2000.18.6.1260.

[7] Humpl T. Neuroblastoma. World Journal of Urology. 13 (4), 1995; 233-239. https://doi.org/10.1007/BF00182969.

[8] Sukumari-Ramesh S, Bentley JN, Laird MD, Singh N, Vender JR, Dhandapani KM. Dietary phytochemicals induce p53- and caspase-independent cell death in human neuroblastoma cells. Int J Dev Neurosci. 29 (7), 2011; 701-710. https://doi.org/10.1016/j.ijdevneu.2011.06.002.

[9] Adiguna SP, Panggabean JA, Atikana A, Untari F, Izzati F, Bayu A, Rosyidah A, Rahmawati SI, Putra MY. pharmaceuticals Antiviral Activities of Andrographolide and Its Derivatives: Mechanism of Action and Delivery System. Pharmaceuticals (basel). 14 (1), 2021; 1102. https://doi.org/10.3390/ph14111102.

[10] Singh SC, Khatri DK, Singh K, Kanchupalli VK, Madan J, Singh SB, Singh H. Molecular encapsulation of andrographolide in 2-hydroxypropyl-β-cyclodextrin cavity: synthesis, characterization, pharmacokinetic and in vitro antiviral activity analysis against SARS-CoV-2. Heliyon. 7(8), 2021; e07741. https://doi.org/10.1016/J.HELIYON.2021.E07741.

[11] Ye L, Wang T, Tang L, Liu W, Yang Z, Zhou J, Zheng Z, Cai Z, Hu M, Liu Z. Poor oral bioavailability of a promising anticancer agent andrographolide is due to extensive metabolism and efflux by P-glycoprotein. J Pharm Sci. 100 (11), 2011; 5007-5017. https://doi.org/10.1002/JPS.22693.

[12] Plubrukarn A, Pinsuwan S, Ingkatawornwong S, Supavita T. Stability of andrographolide in powdered andrographis herb under accelerated conditions. Planta Med. 72 (10), 2006; 72. https://doi.org/10.1055/s-2006-946696.

[13] Tran QTN, Tan WSD, Wong WSF, Chai CLL. Polypharmacology of andrographolide: Beyond one molecule one target. Nat Prod Rep. 38 (4), 2021; 682-692. https://doi.org/10.1039/d0np00049c.

[14] Casamonti M, Risaliti L, Vanti G, Piazzini V, Bergonzi MC, Bilia AR. Andrographolide Loaded in Micro- and Nano-Formulations: Improved Bioavailability, Target-Tissue Distribution, and Efficacy of the "King of Bitters." Engineering. 5 (1), 2019; 69–75. https://doi.org/10.1016/J.ENG.2018.12.004.

[15] Gao H, Su Y, Wang W, Xiong W, Sun X, Ji Y, Yu H, Li H, Oyuang D. Integrated computer-aided formulation design: A case study of andrographolide/ cyclodextrin ternary formulation. Asian J Pharm Sci. 16 (4), 2021; 494–507. https://doi.org/10.1016/J.AJPS.2021.03.006.

[16] Akhtar N, Mohammed SAA, Khan RA, Yusuf M, Singh V, Mohammed HA, Al-Omar MS, Abdellatif Ahmed AH, Naz M, Khadri H. Self-Generating nano-emulsification techniques for alternatively-routed, bioavailability enhanced delivery, especially for anti-cancers, anti-diabetics, and miscellaneous drugs of natural, and synthetic origins. J Drug Deliv Sci Technol. 58, 2020. https://doi.org/10.1016/J.JDDST.2020.101808.

[17] Shariare MH, Kazi M, (Eds.). Phospholipid Based Nano Drug Delivery Systems of Phytoconstituents. Smart Drug Delivery, 2021. https://doi.org/10.5772/INTECHOPEN.101040.

[18] Yang B, Dong Y, Wang F, Zhang Y. Nanoformulations to Enhance the Bioavailability and Physiological Functions of Polyphenols. Molecules. 25 (20), 2020; 4613. https://doi.org/10.3390/MOLECULES25204613.

[19] Damle M, Mallya R. Development and Evaluation of a Novel Delivery System Containing Phytophospholipid Complex for Skin Aging. AAPS PharmSciTech. 17 (3), 2016; 607–617. https://doi.org/10.1208/S12249-015-0386-X/FIGURES/5.

[20] Weers JG, Tarara TE, Dellamary LA, Riess JG, Schutt EG. Phospholipid-based powders for drug delivery. Phospholipid-based powders for drug delivery. WO/2001/085136, 2001.

[21] Hoogevest PV, Wendel A. The use of natural and synthetic phospholipids as pharmaceutical excipients. Eur J Lipid Sci Technol. 116 (9), 2014; 1088-1107. https://doi.org/10.1002/ejlt.201400219.

[22] Telange DR, Sohail NK, Hemke AT, Kharkar PS, Pethe AM. Phospholipid complex-loaded self-assembled phytosomal soft nanoparticles: evidence of enhanced solubility, dissolution rate, ex vivo permeability, oral bioavailability, and antioxidant potential of mangiferin. Drug Deliv Transl Res. 11 (3), 2021; 1056-1083. https://doi.org/10.1007/S13346-020-00822-4.

[23] El-Far SW, Helmy MW, Khattab SN, Bekhit AA, Hussein AA, Elzoghby AO. Phytosomal bilayer-enveloped casein micelles for codelivery of monascus yellow pigments and resveratrol to breast cancer. Nanomedicine (Lond). 13 (5), 2018;481-499. https://doi.org/10.2217/NNM-2017-0301.

[24] Freag MS, Saleh WM, Abdallah OY. Self-assembled phospholipid-based phytosomal nanocarriers as promising platforms for improving oral bioavailability of the anticancer celastrol. Int J Pharm. 535 (1-2), 2018; 18-26. https://doi.org/10.1016/J.IJPHARM.2017.10.053.

[25] Cai X, Luan Y, Jiang Y, Song A, Shao W, Li Z, Zhao Z. Huperzine A-phospholipid complex-loaded biodegradable thermosensitive polymer gel for controlled drug release. Int J Pharm. 433 (1-2), 2012; 102-111. https://doi.org/10.1016/j.ijpharm.2012.05.009.

[26] Maiti K, Mukherjee K, Gantait A, Ahamed HN, Saha BP, Mukherjee PK. Enhanced Therapeutic Benefit of Quercetin–Phospholipid Complex in Carbon Tetrachloride– Induced Acute Liver Injury in Rats: A Comparative Study. Iran J Pharmacol Ther. 4 (2), 2005. (RIDR) IJPT 2005;405.

[27] Maiti K, Mukherjee K, Gantait A, Saha BP, Mukherjee PK. Curcumin-phospholipid complex: Preparation, therapeutic evaluation and pharmacokinetic study in rats. Int J Pharm. 330 (1-2), 2007; 155-163. https://doi.org/10.1016/j.ijpharm.2006.09.025.

[28] Semalty A, Semalty M, Singh D, Rawat MSM. Preparation and characterization of phospholipid complexes of naringenin for effective drug delivery. J Incl Phenom Macrocycl Chem. 67, 2010; 253-260. https://doi.org/10.1007/s10847-009-9705-8.

[29] Semalty A, Semalty M, Rawat BS, Singh D, Rawat MSM. Pharmacosomes: The lipid-based new drug delivery system. Expert Opin Drug Deliv. 6 (6), 2009; 599-612. https://doi.org/10.1517/17425240902967607.

[30] Guo B, Liu H, Li Y, Zhao J, Yang D, Wang X, Zhang T. Application of phospholipid complex technique to improve the dissolution and pharmacokinetic of probucol by solvent-evaporation and co-grinding methods. Int J Pharm. 474 (1-2), 2014; 50-56. https://doi.org/10.1016/j.ijpharm.2014.08.006.

[31] Kim S, Chen J, Cheng T, Gindulyte A, He J, He S, Li Q, Shoemaker BA, Thiessen PA, Yu B, Zaslavsky L, Zhang J, Bolton EE. PubChem in 2021: New data content and improved web interfaces. Nucleic Acids Res. 49 (1), 2021; 1388-1395. https://doi.org/10.1093/nar/gkaa971.

[32] Lee C, Yang W, Parr, GR. Development of the Colic-Salvetti correlation-energy into a functional of the electron density. Phy Rev B Condens Matter. 37 (2), 1988; 785-789. https://doi.org/10.1103/physrevb.37.785.

[33] Breneman CM, Wiberg KB. Determining atom-centered monopoles from molecular electrostatic potentials. The need for high sampling density in formamide conformational analysis. J Comput Chem. 11 (3), 1990; 361-373. https://doi.org/10.1002/jcc.540110311.

[34] Wang J, Wang W, Kollman PA, Case DA. Automatic atom type and bond type perception in molecular mechanical calculations. J Mol Graph Model. 25 (2), 2006; 247-260. https://doi.org/10.1016/j.jmgm.2005.12.005.

[35] Case DA, Betz RM, Cerutti DS, Cheatham TE, Darden TA, Duke RE, Giese TJ, Gohlke H, Goetz AW, Homeyer N, Izadi S, Janowski P, Kaus J, Kovalenko A, Lee TS, LeGrand S, Li P, Lin C, Luchko T, Luo R, Madej B, Mermelstein D, Merz KM, Monard G, Nguyen H, Nguyen HT, Omelyan I, Onufriev A, Roe DR, Roitberg A, Sagui C, Simmerling CL, Botello-smith WM, Swails J, Walker RC, Wang J, Wolf RM, Wu X, Xiao L, Kollman PA. Amber 2016 Reference Manual (Covers Amber16 and AmberTools16). 2016, University of California, San Francisco.

[36] Wang J, Wolf RM, Caldwell JW, Kollman PA, Case DA. Development and testing of a general amber force field. J Comput Chem. 25 (9), 2004; 1157-1174. https://doi.org/10.1002/JCC.20035.

[37] Jorgensen WL, Chandrasekhar J, Madura JD, Impey RW, Klein ML. Comparison of simple potential functions for simulating liquid water. J Chem Phys. 79, 1983; 926-935. https://doi.org/10.1063/1.445869.

[38] Berman HM, Westbrook J, Feng Z, Gilliland G, Bhat TN, Weissig H, Shindyalov IN, Bourne PE. The Protein Data Bank (www.rcsb.org). Nucleic Acids Res. 28 (1), 2000; 235-242. https://doi.org/10.1093/nar/28.1.235

[39] Šali A, Blundell TL. Comparative protein modelling by satisfaction of spatial restraints. J Mol Biol. 234 (4), 1993; 779-815. https://doi.org/10.1006/jmbi.1993.1626.

[40] Meng EC, Pettersen EF, Couch GS, Huang CC, Ferrin TE. Tools for integrated sequence-structure analysis with UCSF Chimera. BMC Bioinformatics. 7, 2006; 339. https://doi.org/10.1186/1471-2105-7-339.

[41] Morris GM, Ruth H, Lindstrom W, Sanner MF, Belew RK, Goodsell DS, Olson AJ. AutoDock4 and AutoDockTools4: Automated docking with selective receptor flexibility. J Comput Chem. 30 (16), 2009; 2785-2791. https://doi.org/10.1002/jcc.21256.

[42] Dolinsky TJ, Czodrowski P, Li H, Nielsen JE, Jensen JH, Klebe G, Baker NA. PDB2PQR: Expanding and upgrading automated preparation of biomolecular structures for molecular simulations. Nucleic Acids Res. 35 (W522-5), 2007. https://doi.org/10.1093/nar/gkm276.

[43] Maier JA, Martinez C, Kasavajhala K, Wickstrom L, Hauser KE, Simmerling C. ff14SB: Improving the Accuracy of Protein Side Chain and Backbone Parameters from ff99SB. J Chem Theory Comput. 11 (8), 2015; 3696-3713. https://doi.org/10.1021/acs.jctc.5b00255.

[44] Machado MR, Pantano S. Split the Charge Difference in Two! A Rule of Thumb for Adding Proper Amounts of Ions in MD Simulations. J Chem Theory Comput. 16 (3), 2020; 1367-1372. https://doi.org/10.1021/acs.jctc.9b00953.

[45] Andersen HC. Rattle: A “velocity” version of the shake algorithm for molecular dynamics calculations. J Comput Phys. 52 (1), 1983; 24-34. https://doi.org/10.1016/0021-9991(83)90014-1.

[46] Darden T, York D, Pedersen L. Particle mesh Ewald: An N·log(N) method for Ewald sums in large systems. J Chem Phys. 98 (12), 1993; 10089-10092. https://doi.org/10.1063/1.464397.

[47] Park HR, Lee H, Park H, Jeon JW, Cho WK, Ma JY. Neuroprotective effects of Liriope platyphylla extract against hydrogen peroxide-induced cytotoxicity in human neuroblastoma SH-SY5Y cells. BMC Complement Altern Med. 15, 2015; 171. https://doi.org/10.1186/s12906-015-0679-3.

[48] Tang H, Zheng Z, Wang H, Wang L, Zhao G, Wang P. Vitamin K2 Modulates Mitochondrial Dysfunction Induced by 6-Hydroxydopamine in SH-SY5Y Cells via Mitochondrial Quality-Control Loop. Nutrients. 14 (7), 2022; 1504. https://doi.org/10.3390/NU14071504.

[49] Wang L, Liu C, Qiao F, Li M, Xin H, Chen N, Wu Y, Liu J. Analysis of the cytotoxic effects, cellular uptake and cellular distribution of paclitaxel-loaded nanoparticles in glioblastoma cells *in vitro*. Exp Ther Med. 21 (4), 2021; 292. https://doi.org/10.3892/etm.2021.9723.

[50] Sriwastva MK, Kunjunni R, Andrabi M, Prasad K, Saxena R, Subbiah V. Neuroprotective effects of activated protein c involve the parp/aif pathway against oxygen-glucose deprivation in sh-sy5y cells. Brain Sci. 10 (12), 2020; 959. https://doi.org/10.3390/brainsci10120959.

[51] Saoji SD, Dave VS, Dhore PW, Bobde YS, Mack C, Gupta D, Raut N. The role of phospholipid as a solubility- and permeability-enhancing excipient for the improved delivery of the bioactive phytoconstituents of Bacopa monnieri. Eur J Pharm Sci. 108, 2017; 108:23-35. https://doi.org/10.1016/J.EJPS.2016.08.056.

[52] Sikarwar MS, Sharma S, Jain AK, Parial SD. Preparation, Characterization and Evaluation of Marsupsin-Phospholipid Complex. AAPS PharmSciTech. 9 (1), 2008; 129-137. https://doi.org/10.1208/s12249-007-9020-x.

[53] Nzai JM, Proctor A. Soy lecithin phospholipid determination by fourier transform infrared spectroscopy and the acid digest/arseno-molybdate method: A comparative study. JAOCS J Am Oil Chem Soc. 76, 1999; 61-66. https://doi.org/10.1007/S11746-999-0048-9.

[54] Chi C, Zhang C, Liu Y, Nie H, Zhou J, Ding Y. Phytosome-nanosuspensions for silybin-phospholipid complex with increased bioavailability and hepatoprotection efficacy. Eur J Pharm Sci. 144, 2020; 105212. https://doi.org/10.1016/J.EJPS.2020.105212.

[55] Petković M, Novak J, Došlić N. Shaping the infrared spectrum of the acetic acid dimer in the OH-stretching range: Multiple conformers and anharmonic coupling. Chem Phys Lett. 474 (4-6), 2009; 248–252. https://doi.org/10.1016/J.CPLETT.2009.04.014.

[56] Liu C, Chen C, Mo H, Ma H, Yuan E, Li Q. Characterization and DPPH radical scavenging activity of gallic acid-lecithin complex. Trop J Pharm Res. 13 (8), 2014; 1333-1338. https://doi.org/10.4314/tjpr.v13i8.19.

[57] Wang J, Arantes PR, Bhattarai A, Hsu RV, Pawnikar S, Huang YM, Palermo G, Miao Y. Gaussian accelerated molecular dynamics: Principles and applications. Wiley Interdiscip Rev Comput Mol Sci. 11 (5), 2021; e1521. https://doi.org/10.1002/wcms.1521.

[58] Wu X, Wang Y, Jia R, Fang F, Liu Y, Cui W. Computational and biological investigation of the soybean lecithin-gallic acid complex for ameliorating alcoholic liver disease in mice with iron overload. Food Funct. 10, 2019; 5203-5214. https://doi.org/10.1039/c9fo01022j.

[59] Roy MJ, Vom A, Okamoto T, Smith BJ, Birkinshaw RW, Yang H, Abdo H, White CA, Segal D, Huang DCS, Baell JB, Colman PM, Czabotar PE, Lessene G. Structure-Guided Development of Potent Benzoylurea Inhibitors of BCL-XLand BCL-2. J Med Chem. 64 (9), 2021; 5447-5469. https://doi.org/10.1021/acs.jmedchem.0c01771

[60] Panariti A, Miserocchi G, Rivolta I. The effect of nanoparticle uptake on cellular behavior: disrupting or enabling functions? Nanotechnol Sci Appl. 5, 2012; 87-100. https://doi.org/10.2147/NSA.S25515.

[61] Rejman J, Oberle V, Zuhorn IS, Hoekstra D. Size-dependent internalization of particles via the pathways of clathrin- and caveolae-mediated endocytosis. Biochem J. 377 (Pt 1), 2004; 159-169. https://doi.org/10.1042/BJ20031253.

[62] Nispa Seetapan; Piyawan Bejrapha; Wanwisa Srinuanchai; Uracha Rungsardthong Ruktanonchai. Rheological and morphological characterizations on physical stability of gamma-oryzanol-loaded solid lipid nanoparticles (SLNs). Micron. 41(1), 2010; 51–58. doi:10.1016/j.micron.2009.08.003.

[63] Albanese, Alexandre; Tang, Peter S.; Chan, Warren C.W. The Effect of Nanoparticle Size, Shape, and Surface Chemistry on Biological Systems. Annu Rev Biomed Eng, 14(1), 2012; 1–16. doi:10.1146/annurev-bioeng-071811-150124.

[64] Vasanth K, Ilango K, MohanKumar R, Agrawal A, Dubey GP. Anticancer activity of Moringa oleifera mediated silver nanoparticles on human cervical carcinoma cells by apoptosis induction. Colloids Surf B Biointerfaces. 117, 2014; 354-359. https://doi.org/10.1016/J.COLSURFB.2014.02.052.

[65] Stoica C, Ferreira AK, Hannan K, Bakovic M. Bilayer Forming Phospholipids as Targets for Cancer Therapy. Int J Mol Sci. 23 (9), 2022; 5266. https://doi.org/10.3390/IJMS23095266/S1.

[66] Baldridge RD, Graham TR. Two-gate mechanism for phospholipid selection and transport by type IV P-type ATPases. Proc Natl Acad Sci U S A. 110 (5), 2013; E358-367. https://doi.org/10.1073/PNAS.1216948110.

[67] Aggarwal V, Tuli HS, Varol A, Thakral F, Yerer MB, Sak K, Varol M, Jain A, Khan MA, Sethi G. Role of R

[68] Valko M, Leibfritz D, Moncol J, Cronin MTD, Mazur M, Telser J. Free radicals and antioxidants in normal physiological functions and human disease. Int J Biochem Cell Biol. 39 (1), 2007; 44-84. https://doi.org/10.1016/J.BIOCEL.2006.07.001

Figures

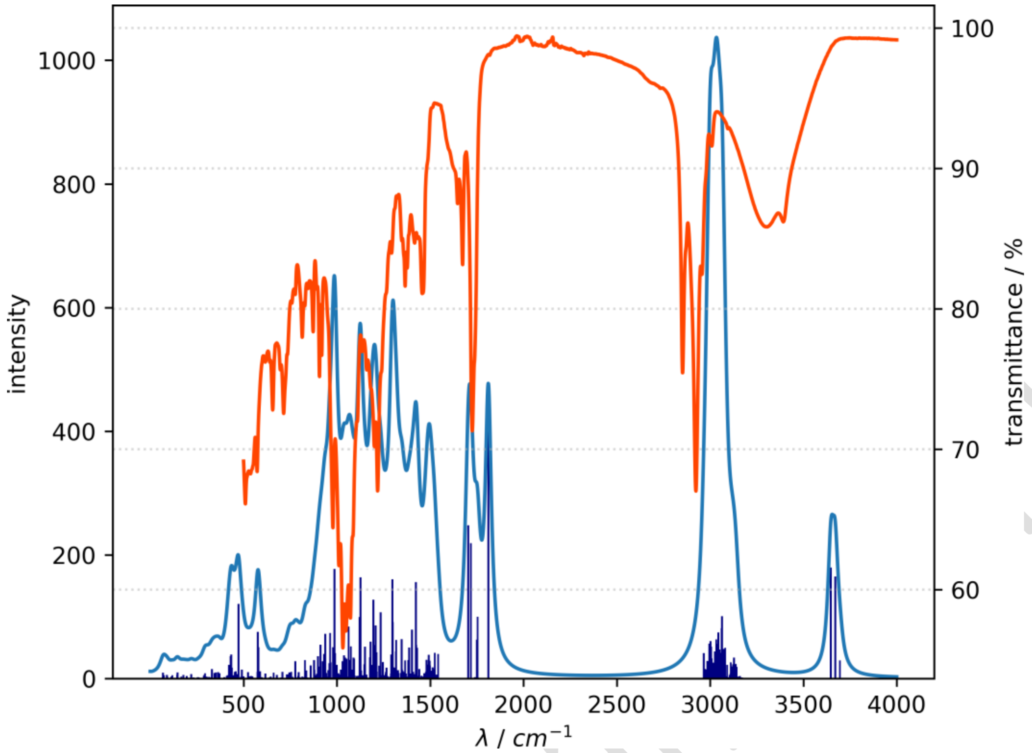

Figure 1: Experimental (red) and calculated (blue) IR spectrum of ANSPC complex calculated at B3LYP/6-311+g(d,p) level of theory. Intensities for all wavenumbers are depicted as stick spectra (navy blue). Predicted spectrum was obtained by convoluting IR transitions by Lorentzian function with full width half maximum of 20 cm^{-1}.

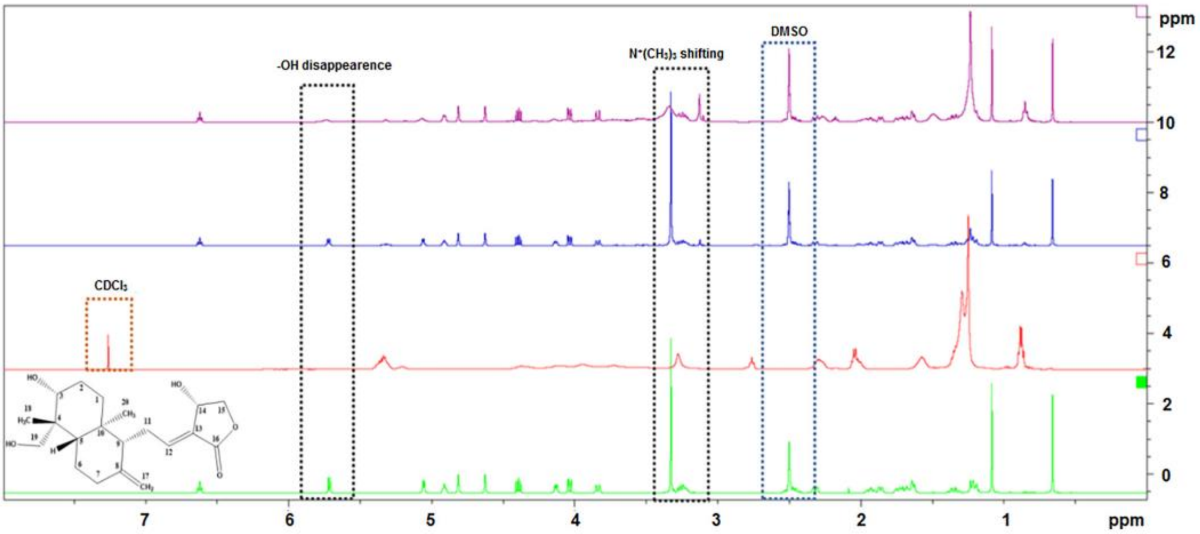

Figure 2:^{1}H NMR spectra for AN (**green**), physical mixture (**blue**) and ANSPC complex (**purple**) in DMSO-d_6 whereas SPC (**red**) in $CDCl_3$.

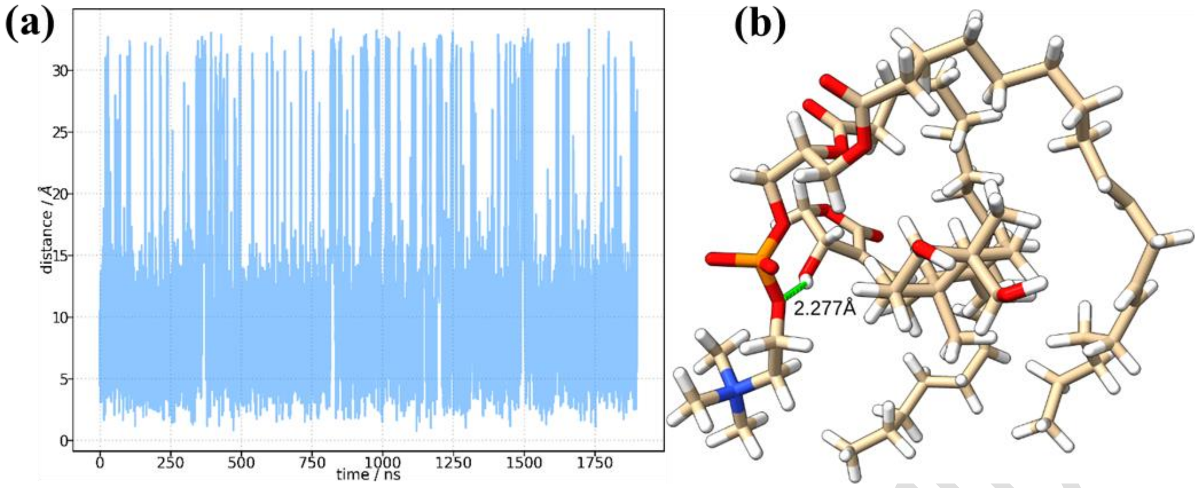

Figure 3: Gaussian-accelerated molecular dynamics (GaMD) simulation of ANSPC complex. Centroid distance between andrographolide (AN) molecules (left). The most appropriate geometry of the ANSPC complex, with centroid distance being 0.76 Å (right).

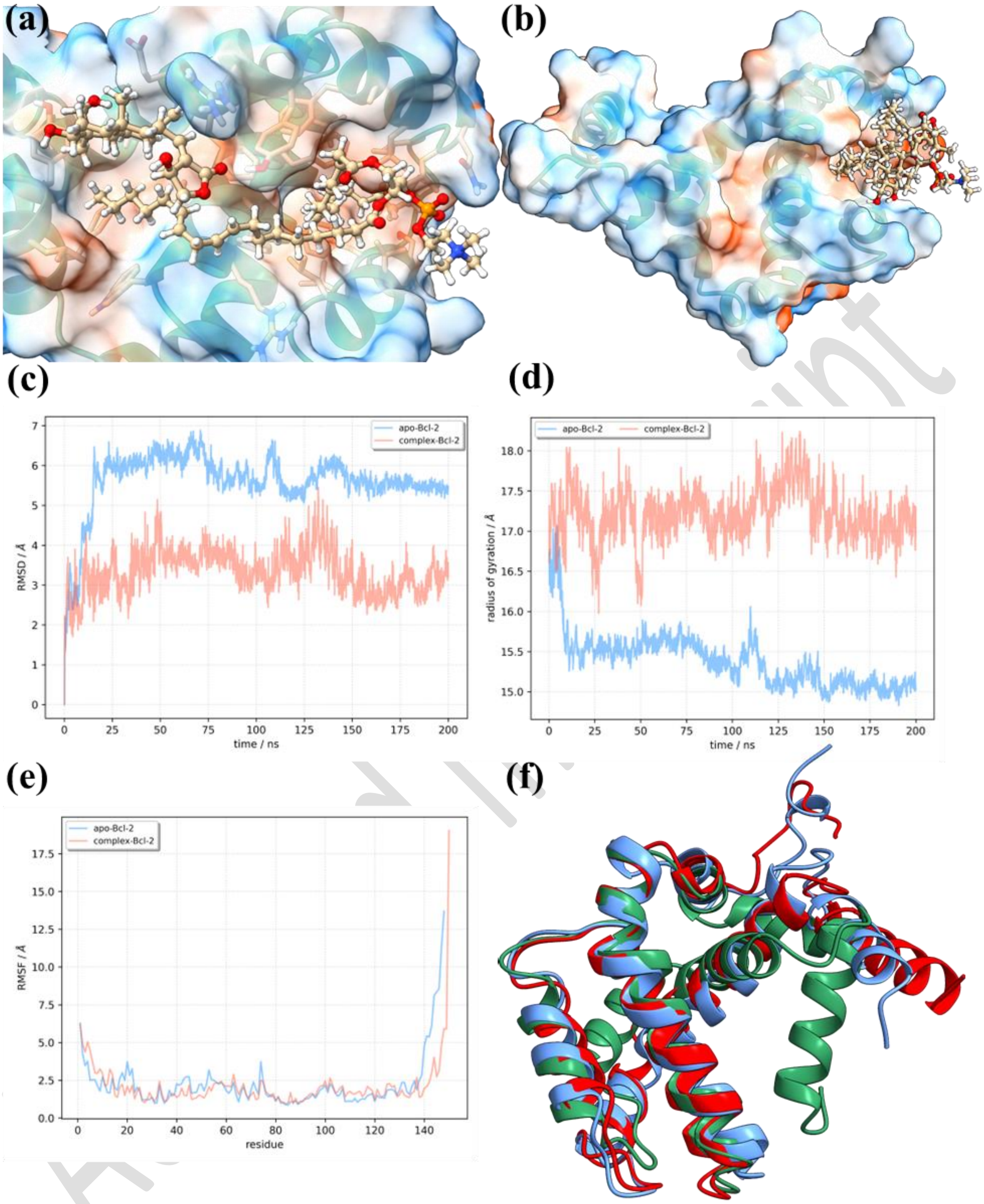

Figure 4: Molecular dynamics simulations of Bcl-2 in Apo- and ANSPC-forms. Initial (a) and final (b) structures of ANSPC-Bcl-2. Evolution of the RMSD (c), radius of gyration (d) and RMSF (e) of the Apo-Bcl-2 (blue) and ANSPC-Bcl-2 (red). Comparison of structures of Bcl-2 (f): crystal structure (PDB ID: 6UVE, red), final structure from the MD simulation of Apo-Bcl-2 (sea green) and complex-Bcl-2 (blue).

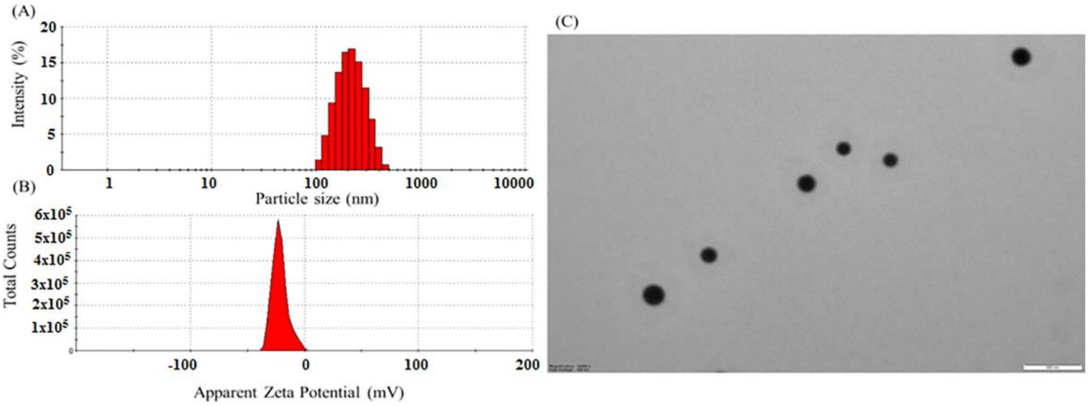

Figure 5: Dynamic light scattering (a); zeta potential (b); and transmission electron microscopy (c); of self-assembled soft ANSPC nanoparticles. Scale bar~500 nm.

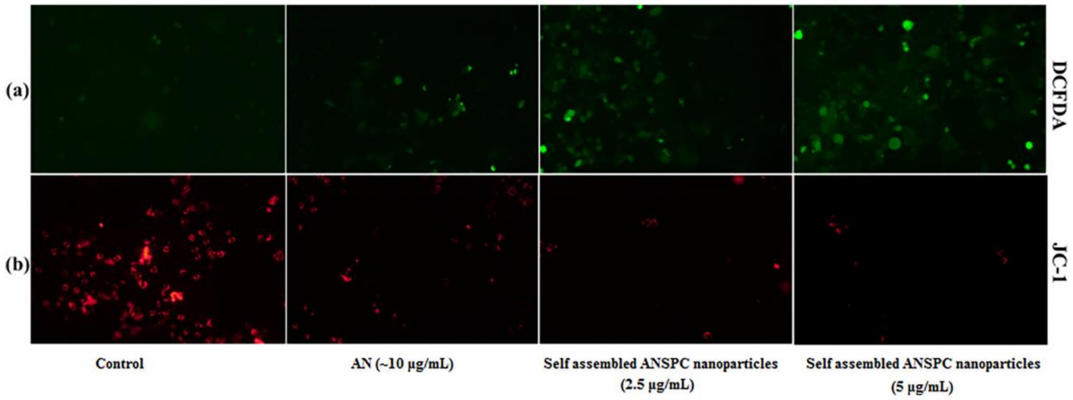

Figure 6: Photomicrographs of fluorescence microscopy of the effect of AN (10-µg/mL) and self-assembled soft ANSPC nanoparticles (2.5-µg/mL and 5-µg/mL) on (a) ROS and (b) MMP (Δψm) production in Neuro2a cells.

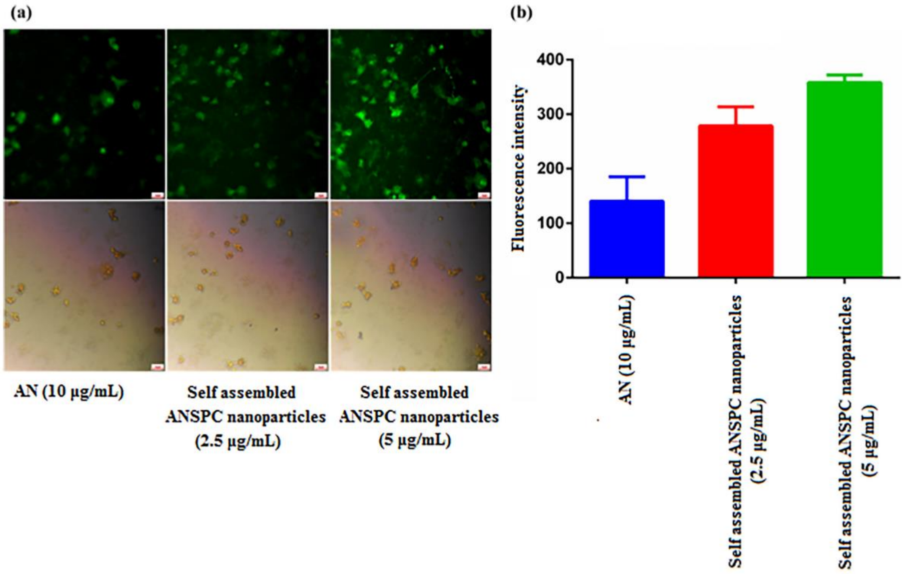

Figure 7: (a) Photomicrographs of fluorescence microscopy representing the internalization of free AN (10-µg/mL) and self-assembled soft ANSPC nanoparticles (2.5-µg/mL and 5-µg/mL); (b) Tubular graph representing the differential changes in fluorescence intensity in Neuro2a cells after treatment with free AN and self-assembled soft ANSPC nanoparticles. All assays were performed in triplicate (n=3) and data were presented as mean ± standard deviations.

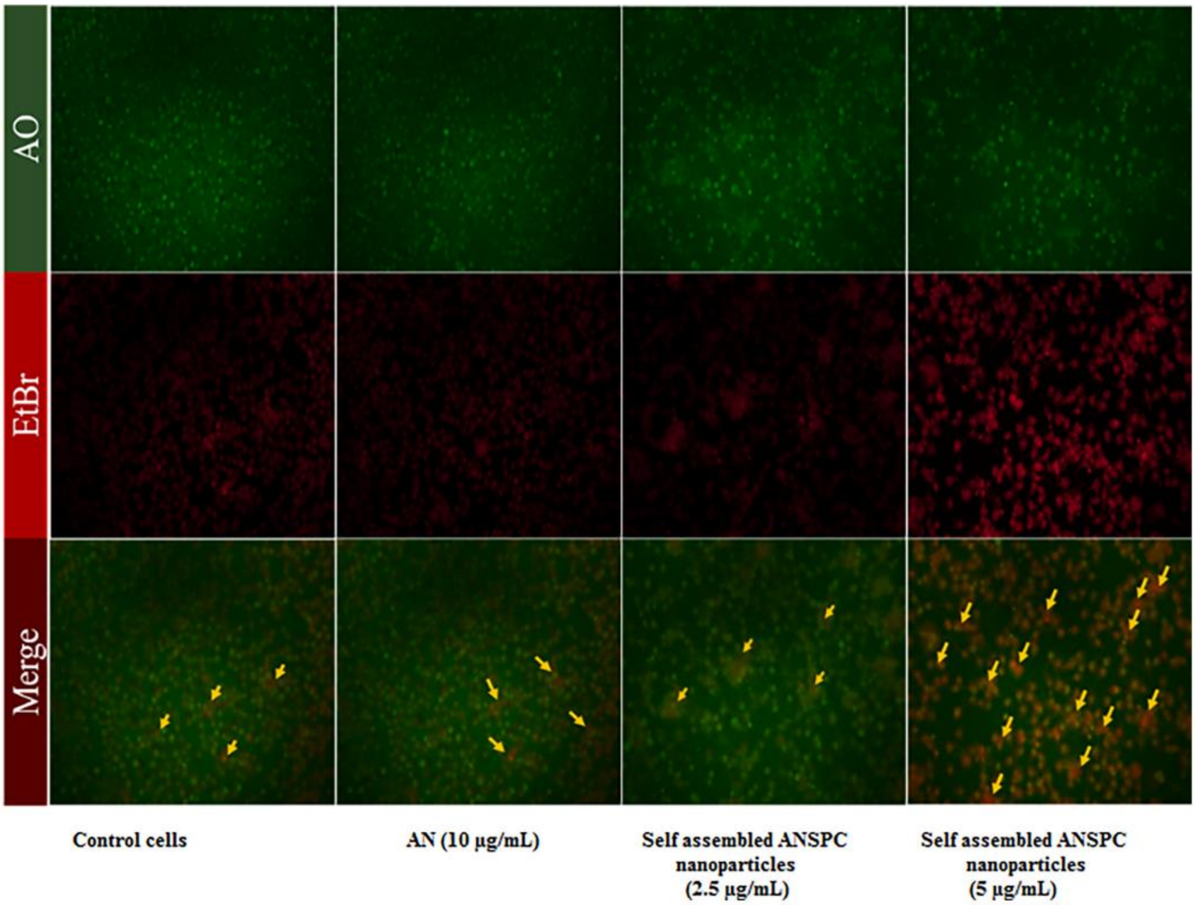

Figure 8: Photomicrographs of fluorescence microscopy of the effect of AN (10-µg/mL) and self-assembled soft ANSPC nanoparticles (2.5-µg/mL and 5-µg/mL) on early apoptotic changes studied using AO/EtBr staining in Neuro2a cells. The fluorescence images were captured in three channels as blue, green and red at 20x magnification. The images reveal the alteration in the morphology of cells after treatment with free AN and self-assembled soft ANSPC nanoparticles.